

PSEUDOCAPACITIVE MECHANISM OF FLEXIBLE MnO_2 ELECTRODES IN NOVEL ROOM TEMPERATURE MOLTEN SALTS ELECTROLYTES INVESTIGATED USING IN-SITU X-RAY ABSORPTION SPECTRA

Ming-Jay Deng ^{1*}, Feng Chen ², Yu-Hsun Hsieh ², and Tzung-Han Chou ^{3*}

ABSTRACT

MnO_2 nanowires were grown on flexible carbon-fiber paper electrodes according to a simple synthesis. The pseudocapacitive behavior of MnO_2 nanowire was tested in various electrolytes. It was found that urea- LiPF_6 room temperature molten salts (RTMS) was the most effective electrolyte to conduct electricity. The ideal MnO_2 supercapacitor electrode, 200 F g^{-1} at 5 mV s^{-1} , was identified. This supercapacitor could perform a wide potential window of 3 V. The energy storage mechanism was graphed in in-situ X-ray absorption spectroscopy (XAS). The urea- LiPF_6 RTMS was proved to provide the functioning ions that stabilize the variation of the Mn valence state during the charging and discharging of RTMS electrolytes. These complementary results could provide scalable and inexpensive applications of high performance reduction/oxidation metal oxide energy storage systems.

Keywords: MnO_2 nanowires; supercapacitor; pseudocapacitive behavior; X-ray absorption spectroscopy; room temperature molten salts.

1. INTRODUCTION

Hybrid electrochemical capacitors (ECs) are efficient energy storage devices that contain the high energy-storage capabilities as batteries and the high power-delivery capabilities as regular capacitors (Conway 1999; Simon and Gogotsi 2008). There is a significant growth in the applications of high-efficient energy storage systems. This is especially true in the manufacturing of electric vehicles, hybrid electric vehicles, and fuel cells (Conway 1999; Simon and Gogotsi 2008; Yang *et al.* 2011; Miller and Simon 2008; Liu *et al.* 2010; Choudhary *et al.* 2017; Wu *et al.* 2010).

In the light of the energy/power densities of ECs depend on the square of the working voltage, the electrolyte with a wide working potential region of stability is indispensable to attain high-efficient energy storage systems, but an improved performance (energy/power densities, cycle-life or safety) of the state of the art ECs is required to fulfill the quickly growing performance claims for these applications. Energy density (E) and power density (P) of an EC are given in the following formulas:

$$E = (C (\Delta V)^2) / 2 \quad (1)$$

$$P = E / t \quad (2)$$

C denotes capacitance, ΔV cell voltage, and t discharging period (Conway 1999). The water decomposition characteristics make the aqueous electrolyte exhibit a narrow potential region (typically $\sim 1 \text{ V}$), thus restraining its EC working voltage. To overcome this problem, researchers assume that RTMS are the electrolytes which can increase the operating voltage of ECs (Armand *et al.* 2009; Wishart 2009; Chang *et al.* 2009; Li *et al.* 2012). ECs combined with RTMS can produce high operating voltage and energy density as a secondary batteries (Liu *et al.* 2010; Zhang and Zhao 2009; Wu *et al.* 2010; Armand *et al.* 2009; Wishart 2009; Chang *et al.* 2009; Li *et al.* 2012). In most cases, an extra Li source is required to supply Li^+ which can be extracted from the electrode during the first charge. This extra Li source in the electrolyte can also increase the rate-performance of a EC by preventing the depletion of ions (e.g., Li^+ or PF_6^-) during the charging and discharging (Armand *et al.* 2009; Wishart 2009; Li *et al.* 2012; Benedetti *et al.* 2008), but this method is usually expensive and unusable in practical applications.

EC technologies are crucial to the development of grid energy storage applications, such as green and smart grid technologies. Green and smart technologies are supposed to produce clean energy from the sources of sun and wind. In order to store all these energies, it will be necessary to develop new efficient energy storage systems (Yang *et al.* 2011). However, three criteria have to be met before new efficient energy storage systems can be built: 1) the materials must be able to produce high performance but low in the price, 2) the materials do not require unusual composition, and 3) the fabrication needs to be scalable and

Manuscript received February 21, 2019; revised June 19, 2019; accepted July 16, 2019.

^{1*} Project Assistant Professor (corresponding author), Bachelor Program in Interdisciplinary Studies, National Yunlin University of Science and Technology, Douliou, Taiwan, 64002, R.O.C. (e-mail: dengmj@yuntech.edu.tw; martinez730523@yahoo.com.tw).

² Master student, Department of Chemical and Materials Engineering, Nation Yunlin University of Science and Technology, Douliou, Taiwan, 64002, R.O.C.

^{3*} Professor (corresponding author), Department of Chemical and Materials Engineering, Nation Yunlin University of Science and Technology, Douliou, Yunlin, Taiwan, 64002, R.O.C. (e-mail: chouth@yuntech.edu.tw).

inexpensive. Considering all the practical factors, incorporating abundant carbon materials on earth with inexpensive MnO_2 seems to be a very promising plan. This incorporation is cost-efficient, and the new energy storage system can take advantage of MnO_2 in its features of pseudo-capacitance and electric double-layer capacitance. MnO_2 is an applicable energy storage material because it is environmentally friendly, abundant in natural resources, and excellent in the performance of charging and discharging (Liu *et al.* 2010). Numerous authors have already studied MnO_2 /carbon composite materials for ECs (Liu *et al.* 2010; Wu *et al.* 2010; Wang *et al.* 2008; Liu *et al.* 2010; Hou *et al.* 2010). As for looking for a suitable electrolyte, RTMS in a binary mixture have remarkably features of low cost, facile accessibility, and friendliness to the environment. They do not require organic solvents. These advantageous features have made RTMS applicable materials in various applications (Tsuda *et al.* 2008; Wang and Zhou 2016; Chen *et al.* 2005; Liang *et al.* 2001; Chen *et al.* 2007). LiPF_6 has been a popular materials in Li-ion batteries because it has voltage stability, outstanding conductivity, and fewer side-effect on our surroundings, we would like to suggest a new material of urea- LiPF_6 RTMS, which is also low-cost and friendly to the environment.

In this study, we will illustrate the fabrication of Birnessite MnO_2 nanowires electrodeposited on carbon-fiber paper (CFP). MnO_2 nanowires will be integrated with the electrolyte of inexpensive Li-ion RTMS composed of LiPF_6 and urea salts. The electrode of MnO_2 nanowire/carbon-fiber paper (MNCFP) will serve as an example because of its great capacitance and rate-capability in aqueous electrolytes. Our research results show that the MNCFP electrode demonstrates a pseudocapacitive behavior in the electrolyte of urea- LiPF_6 RTMS with a voltage range of 3 V. This voltage range has an energy density four to seven times stronger than the integration of MNCFP electrode with other electrolytes, such as aqueous KCl, N-butyl-N-methyl pyrrolidinium-bis(trifluoromethyl-sulfonyl)imide (BMP-TFSI), and LiTFSI-doped RTMS. We will also illustrate the charge-storage mechanism and the variation of Mn oxidation state in MNCFP electrode in various electrolytes, graphed in-situ XAS. This EC can be displayed not only reversibly at operating voltage of 3 V but also in charge-compensation of $\text{Mn}^{3+}/\text{Mn}^{4+}$ reaction, with ~ 0.7 variation of the oxidation state. The maximum specific capacitance (200 F g^{-1} in 3 V) of MNCFP electrode in a urea- LiPF_6 RTMS electrolyte is greater than those reported in the literature (Chang *et al.* 2009; Li, *et al.* 2012; Benedetti *et al.* 2008). Moreover, it exhibits an acceptable cycling performance of $\sim 91.2\%$ retention after 2000 cycles. (All calculations of energy density will exclude the mass of the carbon-fiber paper.)

2. MATERIALS AND METHODS

2.1 MNCFP Electrode preparation

A commercially available CFP (CeTech Co., Taiwan) was used as the substrate to load MnO_2 , with the specifications of weave plain thickness 0.3 mm. MnO_2 nanowires were electroplated onto the CFP in a solution of $0.3\text{M Mn}(\text{CH}_3\text{COO})_2 + 0.2\text{M Na}(\text{CH}_3\text{COO})$ containing a varied concentration of dimethyl sulfoxide (DMSO) under galvanostatic condition 1 mA cm^{-2} at 50°C , in order to produce a total passed charge 300 mC cm^{-2} . Then the nanowires were rinsed with distilled water. The mass of the deposited MnO_2 was approximately 0.2 mg/cm^2 , obtained

from a microbalance with an accuracy of 0.01 mg. A saturated calomel electrode (SCE) and a spiral Pt wire were used to serve as the reference electrode and the counter electrode. Transmission electron microscope (TEM, JEOL 2000F) and scanning electron microscope (SEM, JEOL 6500F) were used to study the morphology and composition of all samples. X-ray diffractometer (XRD, Rigaku MiniFlex II) with a Cu target was used to measure the crystallinity.

2.2 RTMS electrolyte preparation

The LiPF_6 -urea RTMS (molar ratio 1/3.6) was prepared from LiPF_6 (Acros Inc., AP) and urea (Acros Inc., 99%), which was dried at 110°C and 55°C for 12 h in vacuum, respectively (Chen *et al.* 2005; Liang, *et al.* 2001; Chen *et al.* 2007). BMP-TFSI RTMS was manufactured and purified following the procedures in the literature (Chang *et al.* 2009). The content of water in the electrolyte was less than 80 ppm measured by Karl-Fischer titration.

2.3 Electrochemical characterization

The electrochemical properties of the MNCFP electrode in urea- LiPF_6 RTMS were measured by cyclic voltammetry (CV) and chronopotentiometry (CP) at 30°C in an argon-purified glove box (MBraun) in which both oxygen and water content were kept below 1.5 ppm. A Pt wire as a reference electrode in RTMS was placed in a glass tube, containing BMP-TFSI RTMS with a ferrocene (Fc) / ferrocenium (Fc^+) as a potential standard (potential $+0.55 \text{ V vs. SHE}$) (Chang *et al.* 2009). A spiral Pt wire as a counter electrode was soaked in the urea- LiPF_6 RTMS. All the applied potential and the current would be operating in an AUTOLAB potentiostat. The changes of the Mn oxidation states during the cycles were graphed with in-situ XAS (Chang *et al.* 2009).

3. RESULTS AND DISCUSSIONS

3.1 Characterization.

The fabrication process for MnO_2 nanowires/CFP electrodes was showed schematically in Fig. 1. First, MnO_2 nanowires were anodically electrodeposited onto porous CFP substrates in solution of $0.3\text{M Mn}(\text{CH}_3\text{COO})_2 + 0.2\text{M Na}(\text{CH}_3\text{COO}) + 10\%$ DMSO with a current density of 1 mA cm^{-2} at 50°C in order to reach a total passed mass of 300 mC cm^{-2} a CFP substrate ($10 \text{ mm} \times 5 \text{ mm}$). As noted, MnO_2 nanowires were loosely dispersed on CFP, forming a nanofoam structure. After the electrodeposition, the MNCFP structure was completed in hydrated state, which would provide an easy and smooth electron conduction. These 3D electrodes, which combined porous CFP as reservoir materials with MnO_2 nanowires as active materials, would increase the contact of cations in the electrolyte and follow the reversible reaction between $\text{Mn}^{3+}/\text{Mn}^{4+}$. Surface morphology was measured by a SEM and TEM, as it was presented in Fig. 2. Figs. 2a, 2b, and 2c showed the SEM images before and after MnO_2 nanowires were electrodeposited on the CFP surface, respectively. These MnO_2 nanowires revealed the porous construction and the great adhesion to CFP surface. They yielded a great electrochemically active surface which had low resistance of the electrode. The electrodes on the surface areas were found to be $30.5 \text{ m}^2 \text{ g}^{-1}$ (bare CFP electrode) and $212.8 \text{ m}^2 \text{ g}^{-1}$ (MNCFP electrode) measured by Brunauer-Emmett-Teller (BET). The active surface

increased significantly because of the coverage of MnO₂ nanowires, which was corresponding to the SEM images. Such a microstructure ensured the optimum utilization of MnO₂ within the diffusion length of the cations.

Figures 2e and 2f showed SEM images of the product prepared under experimental conditions similar to those for MNCFP. However, various amounts of DMSO were added in the sample electrolytes. In the electrolyte with 10% DMSO, whisker, rod structures of varied nanosizes with small porosity were observed, but the deposits became less uniform and had less microporous architectures. Surface area of the sample electrodes was determined to be 147.1 m² g⁻¹ in the electrolyte with 5% DMSO and 76.3 m² g⁻¹ in the electrolyte without DMSO. This highly porous nanofoam structure (*i.e.*, with 10% DMSO in the electrolyte) constituted in MnO₂ nanowires and porous CFP could be a candidate with strong potential in the applications of EC electrodes.

The XRD patterns of MNCFP electrodes were fabricated with DMSO in varied concentrations in the electrolyte and CFP substrate, respectively (Fig. 3a). The patterns of the electrodes with DMSO in varied concentrations displayed no significant diffraction signals matched to MnO₂; all significant signals were accompanied with graphite. Broad or weak signals were associated with a poorly crystallized MnO₂ coming from the amorphous carbon effect. To elucidate the local structure of MNCFP, we applied Raman and TEM, which was sensitive to the short range order amorphous materials. Figure 3b displayed the spectrum of MNCFP and bare CFP electrode. Three primary peak

matched to MnO₂ could be determined at 500, 575 and 648 cm⁻¹. The region (648 cm⁻¹) could be recognized as the Mn-O symmetric stretching vibration of the MnO₆, and the second region situated at 575 cm⁻¹ could be recognized as the Mn-O stretching vibration in the plane of MnO₆ (Julien *et al.* 2003). According to these vibrational characteristics, the Birnessite type MnO₂ could be established. TEM image of MnO₂ nanowires was showed in Fig. 2d. It was constituted in interweaving nanowires (~ 30 nm diameter).

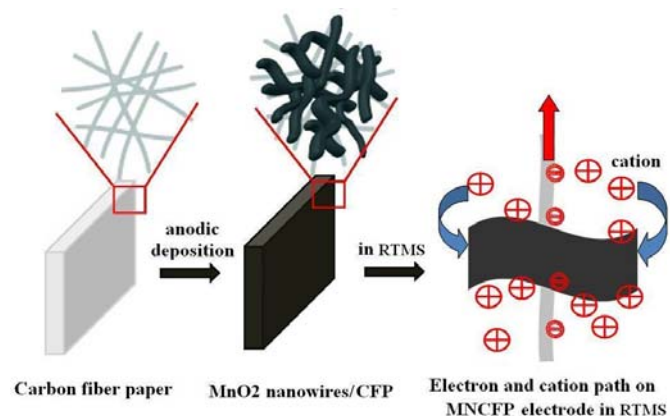


Fig. 1 Schematic diagram of fabrication a MNCFP hybrid electrode.

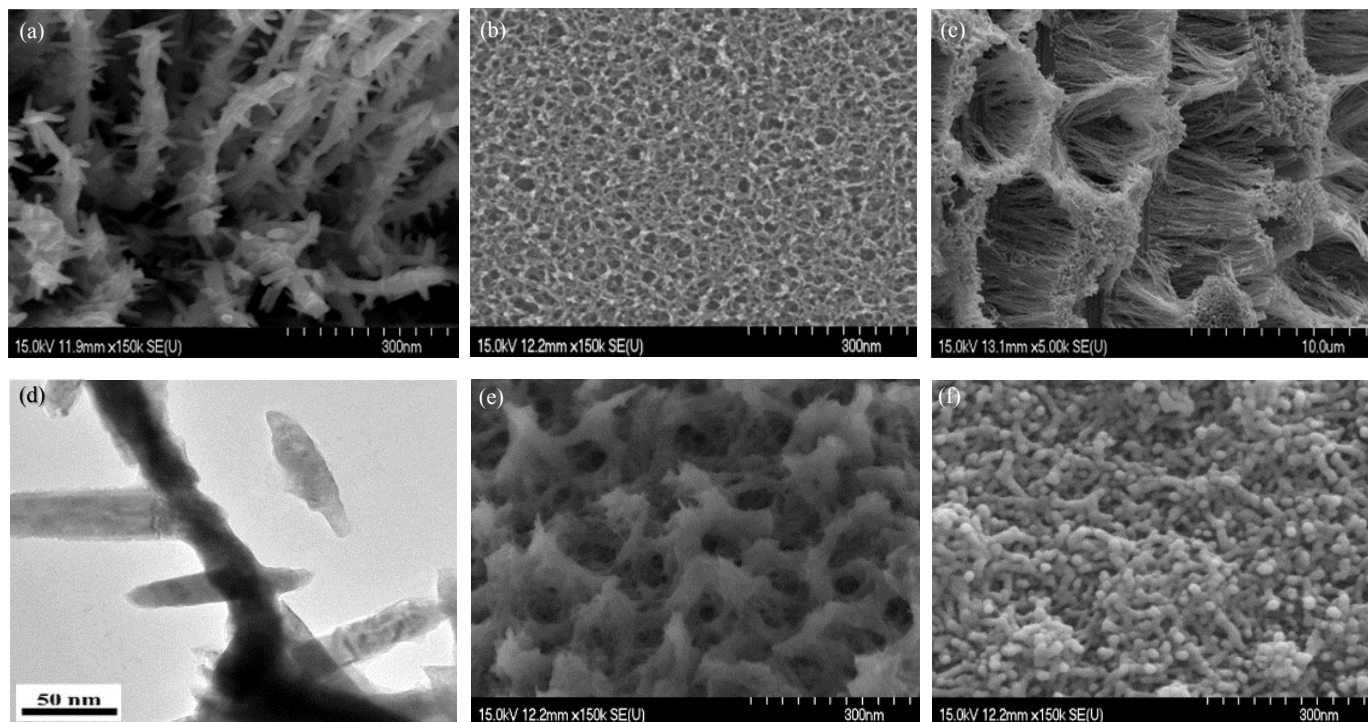


Fig. 2 (a) SEM image of the CFP surface before the deposition of MnO₂; (b) and (c) SEM images of the MNCFP electrodes prepared in solution of 0.3M Mn(CH₃COO)₂ + 0.2M Na(CH₃COO) + 10% DMSO with current density 1 mA cm⁻² at 50°C to produce a total passed charge 300 mC cm⁻² at various magnifications; (d) TEM image of the MnO₂ nanowires; (e) SEM images of the whisker-like MnO₂ electrode prepared in solution of 0.3M Mn (CH₃COO)₂ + 0.2M Na(CH₃COO) + 5% DMSO at current density 1 mA cm⁻² at 50°C; (f) SEM images of the nanostructure MnO₂ electrode prepared in solution of 0.3M Mn(CH₃COO)₂ + 0.2M Na(CH₃COO) without DMSO with a current density of 1 mA cm⁻² at 50°C to produce a total passed charge of 300 mC cm⁻².

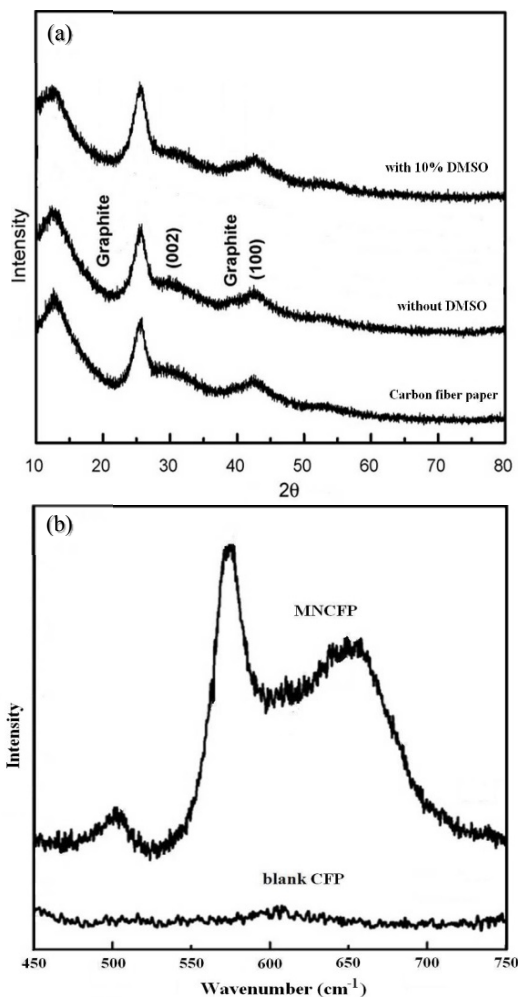


Fig. 3 (a) XRD patterns of the MNCFP hybrid electrodes with varied concentrations of DMSO. (b) Raman spectra of MNCFP and CFP electrodes.

3.2 Electrochemical Characterization.

The potential windows of the manufactured RTMS electrolytes were measured with CV. An attempt to use an aprotic RTMS as an electrolyte was also made. Curve (a) in Fig. 4 exhibited a wide working window of BMP-TFSI RTMS, extending from approximately -3.3 V to $+2.3$ V, in which the cation reduction and the anion oxidation occurred and caused decomposition of the RTMS. A great working window (~ 5.5 V), comparing to other common aqueous solutions (~ 1 V), would make RTMS a potential electrolyte in high voltage energy storage systems. However, the small current on the background might be related to electrolysis or decomposition of few impurity in RTMS. Addition of LiTFSI to the RTMS was found not to alter the CV shape (curve b), indicating that the Li^+ reduction was outside of the potential range. Accordingly, carbon-based EC incorporating RTMS in a large cell voltage had been proposed (Liu *et al.* 2010; Zhang *et al.* 2008; Lewandowski *et al.* 2004; Merlet *et al.* 2012). The CV shape of the MNCFP electrode in blank BMP-TFSI RTMS was presented in Fig. 5a. A quasi-rectangular CV was observed (while a little distorted), indicating an electrochemical capacitive behavior of MNCFP in blank BMP-TFSI RTMS electrolyte.

Specific capacitance (C) of MnO_2 was measured with this equation:

$$C = Q_m / \Delta V \quad (3)$$

Q_m denoted the charge collected from the CV (depended on weight), and ΔV the working voltage (or the scanning range). The calculated result showed that the C was 32 F g^{-1} in blank BMP-TFSI RTMS at 5 mV s^{-1} . As the BET of the MNCFP electrode was estimated to be $212.8 \text{ m}^2 \text{ g}^{-1}$, the double layer capacitance in RTMS was only about $10 \text{ } \mu\text{F cm}^{-2}$ (Lewandowski *et al.*, 2004). This C value (32 F g^{-1}) was too large to be merely considered to be double layer capacitance; a pseudocapacitive behavior of MnO_2 was hence anticipated. The LiTFSI was then added in BMP-TFSI RTMS, in an attempt to increase the performance of MNCFP electrode. As shown in Fig. 5b, the capacitive behavior revealed in the CV could be considered as a reversible redox reaction of MnO_2 in 2 V (from -1.5 V to $+0.5$ V). In the 2V region, the CV current was nearly consistent during forward and backward scanning. However, a straightway changed its path when the applied potential was inverted. The working potential of MnO_2 in LiTFSI-doped RTMS, approximately 2 V, was twice as much as that of other common aqueous electrolytes. It would enable the pseudocapacitor to operate in a high voltage. Its energy/power density could therefore be enhanced on the basis of Eqs. (1) and (2). The area of the CV in Fig. 5b was greater than that of Fig. 5a, showing a higher charge storage capacity of MNCFP in LiTFSI-doped RTMS. The C value was improved from 32 to 90 F g^{-1} when 0.01M LiTFSI was added to RTMS electrolyte, indicating that MnO_2 redox reactions were operative in RTMS. Figure 5c summarized the C values of MnO_2 as a function of Li^+ concentration in BMP-TFSI RTMS. This result indicated that the introduced small cation, Li^+ , could join the insertion and de-insertion processes and conduce a small, additional capacitance. However, too much doping might lead to a converse effect. This converse effect could be found in data of the ionic conductivity. Figure 5d displayed the change of the RTMS ionic conductivity in different LiTFSI concentrations. A monotonically decreasing conductivity was found, and the conductivity then increased according to the extent of doping. The viscosity of the electrolyte was also found to increase progressively according to Walden's rule.

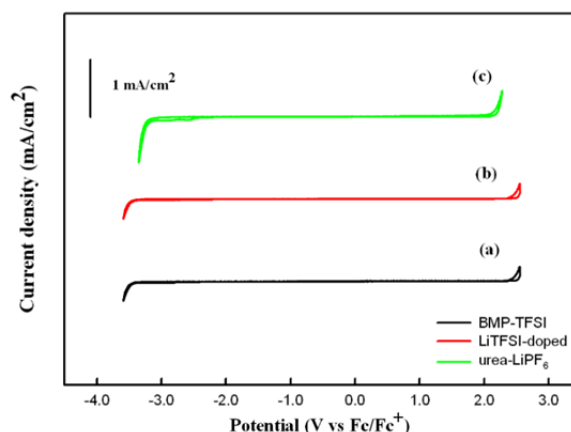


Fig.4 Cyclic voltammograms of an inert glassy carbon electrode recorded in blank BMP-TFSI (curve a), LiTFSI-doped (curve b), and blank urea- LiPF_6 (curve c) melt, at a potential scan rate of 10 mV s^{-1} .

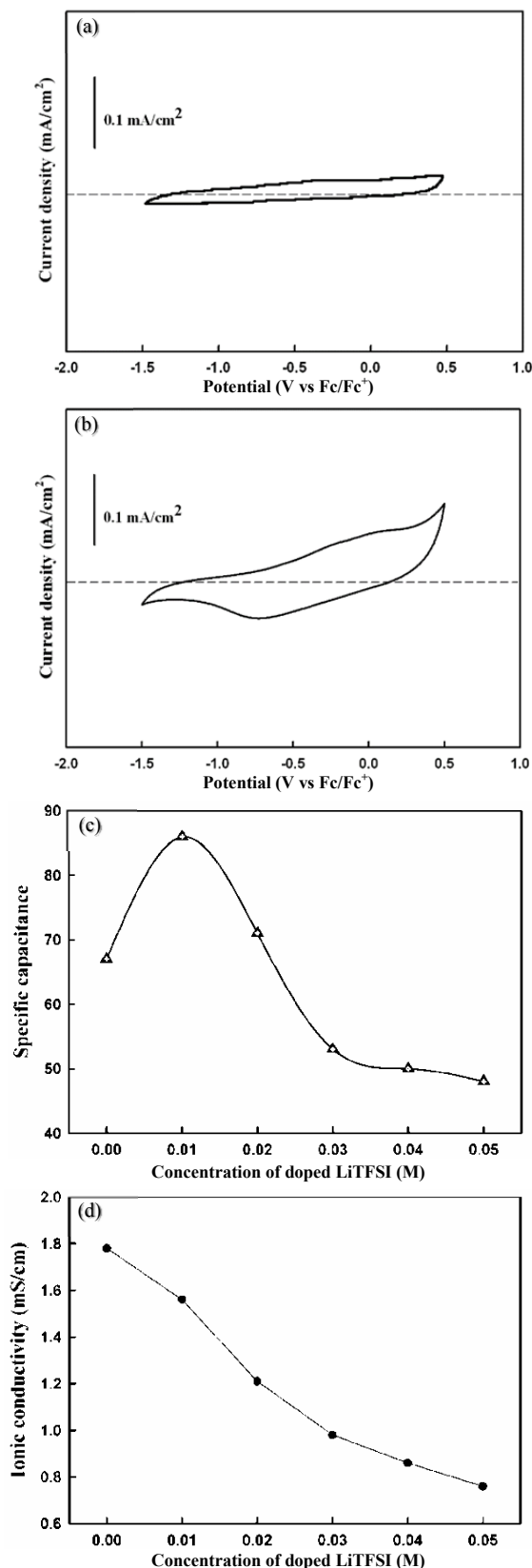


Fig.5 Cyclic voltammograms of the MNCFP electrode measured in (a) blank BMP-TFSI and (b) LiTFSI-doped RTMS at a potential scan rate of 5 mV s⁻¹. (c) MNCFP electrode capacitances as a function of the LiTFSI concentration in BMP-TFSI RTMS (d) Variation of ionic conductivity of the BMP-TFSI RTMS doped with concentrations of LiTFSI.

Curve c in Fig. 4 displayed the acquired CV tested in blank urea-LiPF₆ RTMS. The working potential window expanded from -3.0 V to +2.0 V (vs. Fc/Fc⁺). Figure 6a showed the CV shape of MNCFP electrode tested in urea-LiPF₆ electrolytes. Figure 6a showed the CV shape of MNCFP electrode tested in the urea-LiPF₆ electrolytes. The 3 V region measured by a wide redox was significantly noticeable, and symmetric integrated charges were also found. The quasi-rectangular CV responses was recognized to be a reversible Mn³⁺/Mn⁴⁺ redox reaction of MnO₂ nanowires in urea-LiPF₆ RTMS. The obtained C values of MNCFP electrode in urea-LiPF₆ RTMS was 200 Fg⁻¹ at 5 mV s⁻¹. A little slanting CV curve could be recognized to be insertion and deinsertion counteractant of charge carriers in or out of MnO₂ (This interpretation would be specified later). Figure 6b showed the chemical structure of the urea-LiPF₆ RTMS. The acquired CP curve of MNCFP electrode during charge/discharge cycling between -1.7 V and +1.3 V (vs. Fc/Fc⁺) was presented in Figs. 6c and 6d, respectively. The large electrode operating range ~ 3.0 V in the urea-LiPF₆ RTMS would allow a greater energy/power density of an EC. It was noteworthy that the performance of MNCFP electrode in the urea-LiPF₆ RTMS electrolyte was remarkably greater than that of the previous research. The performance of graphene ECs were found to have < 136 W h kg⁻¹ (Wang *et al.* 2008; Liu *et al.* 2010). MnO₂ nanowires/graphene composite (MNGC) ECs were found to have ~ 30 W h kg⁻¹ (Wu *et al.* 2010). Activated carbon ECs were found to have < 10 W h kg⁻¹ (Wang *et al.* 2008). More other electrolyte MnO₂-based pseudocapacitors were found to have lower performance (Chang *et al.* 2009; Li *et al.* 2012; Benedetti *et al.* 2008; Wang *et al.* 2008; Liu *et al.* 2010; Hou *et al.* 2010). In Fig. 6d, we matched the energy/power densities of MNCFP in 0.01M LiTFSI-doped RTMS, urea-LiPF₆ RTMS, and 3M KCl aqueous solution at 30°C, respectively. Energy/power densities were derived from MNCFP electrodes charge-discharge curves tested at different rates. The maximum energy densities of MNCFP electrodes in 0.01M LiTFSI-doped RTMS, urea-LiPF₆ RTMS, and 3M KCl aqueous solution were 50, 250, and 50.6 W h kg⁻¹.

With MNCFP electrode in the urea-LiPF₆ RTMS, not only did the C values increase from 90 to 270 F g⁻¹ but also the operating voltage range increased from 2 V to 3 V. The energy /power densities, according to Eqs. (1) and (2), were obtained from the CP tested at different scan rates. Using MNCFP electrode in the urea-LiPF₆ electrolyte for ECs was very promising in the applications that required high energy and operated at high temperatures.

To measure the charge/discharge durability of MNCFP electrode in urea-LiPF₆ RTMS, 2000 redox CP cycles was conducted (Fig. 7). The retained capacitance was as great as 91.2%, comparing to the initial value from the 1st cycle. The capacitance C remained nearly unchanged without further decline after 500 cycles. The reasons for this phenomenon were not fully comprehended. Further investigation would be needed. In contrast, in 3M KCl aqueous solution, only 81.7% of the original C values could be kept after 500 cycles; this waning was attributed mostly to fractional MnO₂ dissolution in the aqueous solution (Chang *et al.* 2004). The great stability and reversibility of the MNCFP electrode in urea-LiPF₆ RTMS were highly related to the chemical benignity of urea-LiPF₆ and to the low solubility of MnO₂ in the electrolyte. The research results concluded that the MNCFP electrode in urea-LiPF₆ RTMS would be a prospective electrolyte for energy storage.

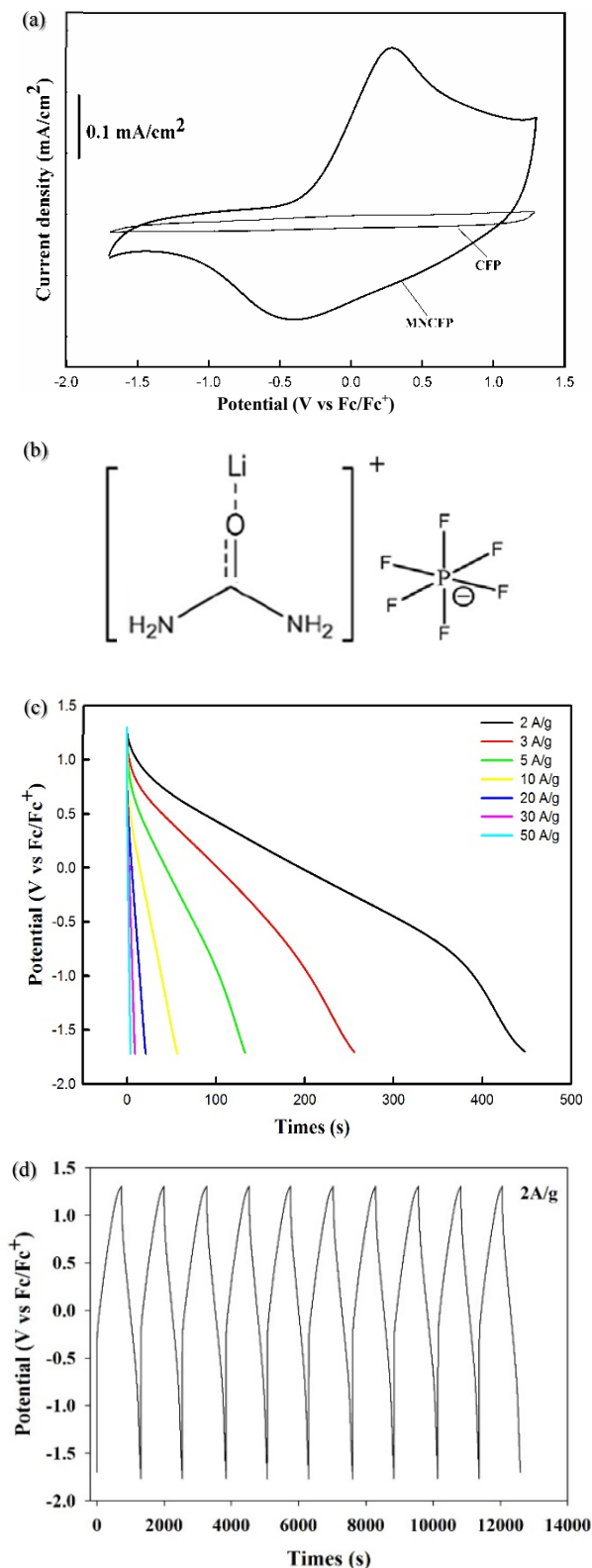


Fig.6 (a) Cyclic voltammograms of MNCFP and CFP without MnO₂ recorded in urea-LiPF₆ RTMS at a potential sweep rate 5 mV s⁻¹. (b) Chemical structure of the urea-LiPF₆ RTMS. (c) CP for discharge cycles of the MNCFP electrode measured in the potential range from -1.7 V to 1.3 V (vs. Fc/Fc⁺) at discharge current density 2 A g⁻¹ ~ 50 A g⁻¹. (d) CP for ten charge-discharge cycles of the MNCFP electrode in urea-LiPF₆ RTMS measured at an applied current density ± 2 A g⁻¹.

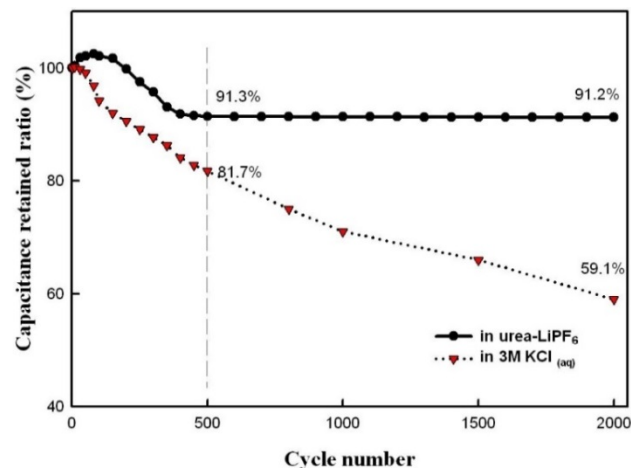


Fig. 7 Variation of MNCFP electrode capacitance vs. CV cycle number measured in urea-LiPF₆ RTMS and 3M KCl aqueous solution.

In-situ Mn K-edge XAS was used to graph the charge storage mechanism and the Mn oxidation state change in urea-LiPF₆ RTMS during charge/discharge cycling. Figure 8a displayed Mn K-edge X-ray Absorption Near Edge Structure (XANES) spectra of MNCFP electrode in urea-LiPF₆ RTMS tested and changed in this order: -1.7, -1.2, -0.7, -0.1, +0.3, +0.8, +1.3, then back to +0.8, +0.3, -0.1, -0.7, -1.2, and finally -1.7V (vs. Fc/Fc⁺). All of these XAS curves displayed a miniature change with growing operating potential, indicating a resemblance in [MnO₆] framework of MnO₂ under different operating potentials. The adsorption growing edge of the XANES spectra were found to move to the greater energy through enhancing operating potential, and nearly backtracked to the early location as the operating potential was reversed, as shown in Fig. 8a. Based on absorption threshold energy (E₀) derived from the XANES in Figure 8a (Chang *et al.* 2009; Belli *et al.* 1980; Ghigna *et al.* 2000), the average Mn oxidation state was determined and presented in Fig. 8b. The reference samples: MnO(II), Mn₂O₃(III), and MnO₂(IV) were measured; the corresponding E₀ was 6544.7 eV, 6548.2 eV, and 6552.6 eV. The change of the Mn oxidation state was approximately between -1.7 V and +1.3 V, which was higher than the voltage range when in-situ XAS was used (Chang *et al.* 2009; Sassin *et al.* 2010; Lee *et al.* 2010).

Figures 8c and 9 displayed the average Mn oxidation state and the XANES spectra obtained below operating potentials/V, respectively. The voltage was revealed in this order: -1.5, +0.5, then -1.5 in BMP-TFSI IL, -1.5, then +0.5, and finally -1.5 (vs. Fc/Fc⁺) in 0.01M LiTFSI-doped IL. The Mn valence changes in BMP-TFSI and in LiTFSI-doped RTMS (0.01 M) were found to fall between -1.5 V and +0.5 V. This voltage range was significantly smaller than the voltage range where the Mn valence would change in the urea-LiPF₆ RTMS. This condition undoubtedly meant a great ionic/electronic conductivity of MNCFP electrode in the urea-LiPF₆ RTMS. A continuous and reversible Mn³⁺/Mn⁴⁺ reaction of MNCFP occurred in the urea-LiPF₆ RTMS that facilitated the high performance in voltage in Fig. 6a. The valid redox reaction brought the outstanding energy density ~ 250 W h kg⁻¹ at the power density of 2.7 kW kg⁻¹ and the energy density of 40 W h kg⁻¹ at the power density 104 kW kg⁻¹ for these electrochemical capacitors.

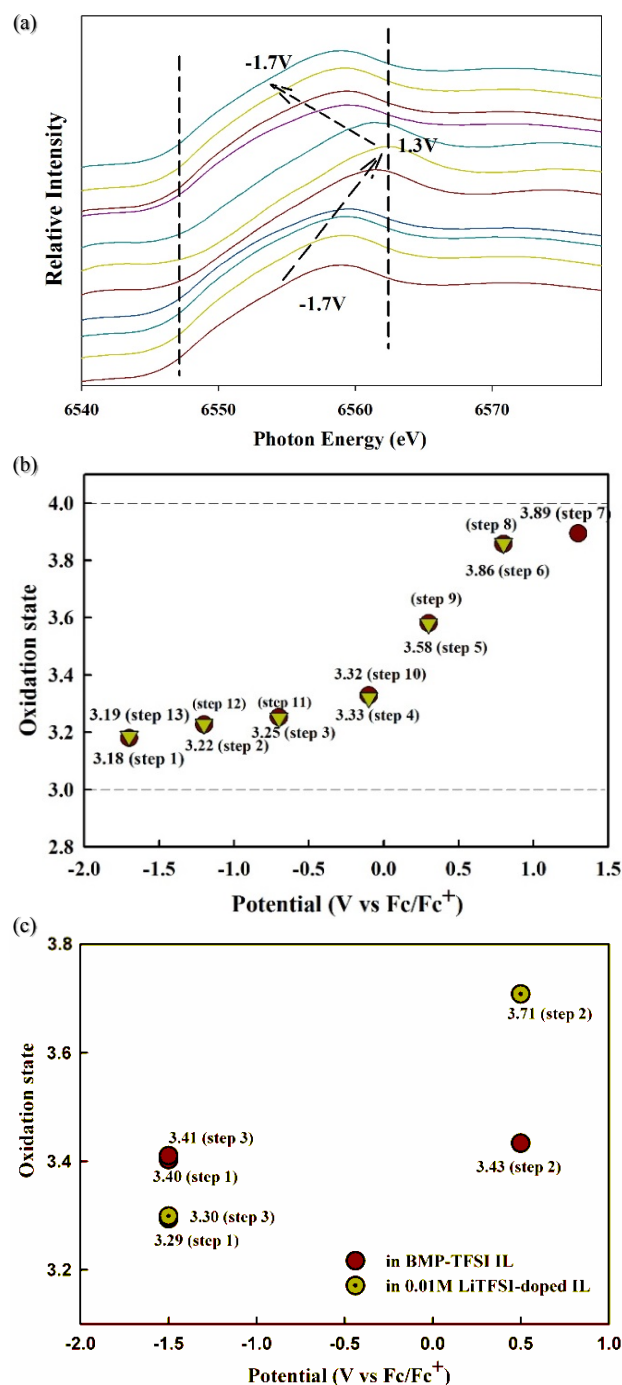


Fig. 8 (a) In-situ Mn K-edge XANES spectra of the MNCP electrode measured in urea-LiPF₆ RTMS. (b) Variation of Mn oxidation state in urea-LiPF₆ RTMS with applied potential. (c) Variation of Mn oxidation state in BMP-TFSI and 0.01M LiTFSI-doped RTMS with applied potential, respectively.

4. CONCLUSION

A brief and common approach effected the synthesis of MnO₂ nanowires /CFP as electrodes linked with a Li-ion melt as electrolytes for EC applications. The MNCFP electrode in the urea-LiPF₆ RTMS electrolyte could operate up to ~ 3 V, and displayed a great *C* value of 200 F g⁻¹. In-situ XAS spectra

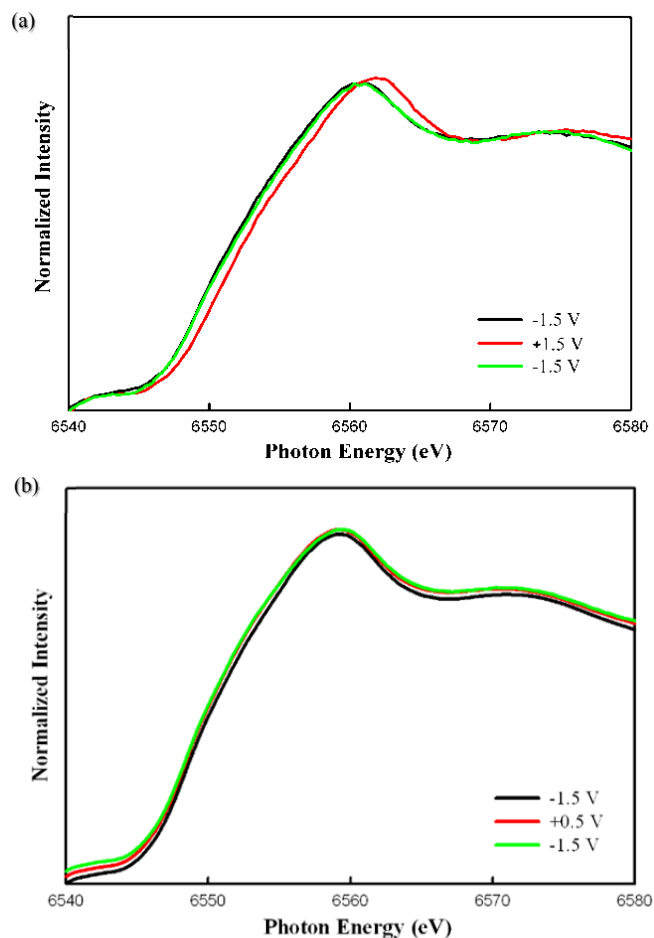


Fig. 9 In-situ Mn K-edge XANES spectra of the MNCFP electrode measured at applied potentials in sequence -1.5V, +0.5V and then back to -1.5V (a) in 0.01M LiTFSI-doped (b) in blank BMP-TFSI RTMS.

graphed the charge storage mechanism in RTMS. The results indicated that the transition of Mn³⁺ and Mn⁴⁺ during charge/discharge cycling was recouped by the reversible Li(urea)_n⁺ insertion into the tunnels between MnO₆ units and the withdrawal from them. In contrast, the BMP⁺ and Li⁺ merely adsorbed on the electrode surface, and did not pass through the tunnels. This work might not only provide a valid method to recognize the mechanism involving the urea-LiPF₆ RTMS electrolyte but also open a new path for the development of efficient systems to store energy using novel RTMS electrolytes.

ACKNOWLEDGMENTS

We would like to thank the National Synchrotron Radiation Research Center (NSRRC) staff for their technical support. The work was supported by the Ministry of Science and Technology (MOST 107-2218-E-224-002-MY2, Taiwan).

COMPETING INTERESTS

The authors declare no competing interests.

REFERENCES

- Chang, Y.-H., Nikam, R.D., Lin, C.-T., Huang, J.-K., Tseng, C.-C., Hsu, C.-L., Cheng, C.-C., Su, C.-Y., Li, L.-J., and Chua, D. H.C. (2014). "Enhanced Electrocatalytic Activity of MoS_x on TCNQ-treated Electrode for Hydrogen Evolution Reaction." *ACS Applied Materials & Interfaces*, **6**, 17679-17685.
- Chang, Y.-H., Zhang, W., Zhu, Y., Han, Y., Pu, J., Chang, J.-K., Hsu, W.-T., Huang, J.-K., Hsu, C.-L., Chiu, M.-H., Takenobu, T., Li, H., Wu, C.-I., Chang, W.-H., Wee, A.T.S., and Li, L.-J. (2014). "Monolayer MoSe₂ Grown by Chemical Vapor deposition for Fast Photodetection." *ACS Nano*, **8**, 8582-8590.
- Chang, Y.-H., Wu, F.-Y., Chen, T.-Y., Hsu, C.-L., Chen, C.-H., Wiryong, F., Wei, K.-H., Chiang, C.-Y., and Li, L.-J. (2014). "Three-Dimensional Molybdenum Sulfide Sponges for Electrocatalytic Water Splitting." *Small*, **10**, 895-900.
- Chang, Y.-H., Lin, C.-T., Chen, T.-Y., Hsu, C.-L., Wei, K.-H., and Li, L.-J. (2013). "Highly Efficient Electrocatalytic Hydrogen Production by MoS_x Grown on Graphene-Protected 3-Dimensional Ni Foam." *Advanced Materials*, **25**, 756-760.
- Cantalini, C., Valentini, L., Lozzi, L., Armentano, I., Kenny, J.M., and Santucci, S. (2003). "NO₂ gas sensitivity of carbon nanotubes obtained by plasma enhanced chemical vapor deposition." *Sensors and Actuators. B, Chemical*, **93**, 333-337.
- Chopra, S., Phama, A., Gaillard, J., Parker, A., and Rao, A.M. (2002). "Carbon-nanotube-based resonant-circuit sensor for ammonia." *Applied Physics Letters*, **80**, 4632-4634.
- Collins, P.G., Bradley, K., Ishigami, M., and Zettl, A. (2000). "Extreme Oxygen Sensitivity of Electronic Properties of Carbon Nanotubes." *Science*, **287**, 1801-1804.
- Chopra, S., McGuire, K., Gothard, N., and Rao, A.M. (2003). "Selective gas detection using a carbon nanotube sensor." *Applied Physics Letters*, **83**, 2280-2282.
- Chang, Y.-H., Lin, H.-W., and Chen, C. (2012). "Growth mechanism of self-assembled TiO₂ nanorod arrays on Si substrates fabricated by Ti anodization." *Journal of The Electrochemical Society*, **159**, D512-D517.
- Chang, Y.-H., Chen, Y.-T., Huang, C.-S., Lu, C.-L., Lee, S.-H., Huang, B.-R., and Chen, C. (2018). "Growth Mechanism of Self-Assembled Ti_xW_yO Nanotubes Fabricated by TiW Alloy Anodization." *Journal of The Electrochemical Society*, **165**, D1-D5.
- Futaba, D.N., Hata, K., Yamada, T., Hiraoka, T., Hayamizu, Y., Kakudate, Y., Tanaike, O., Hatori, H., Yumura, M., and Iijima, S. (2006). "Shape-engineerable and highly densely packed single-walled carbon nanotubes and their application as super-capacitor electrodes." *Nature Materials*, **5**, 987-994.
- George, R., Kashyap, K., Rahul, R., and Yamdagni, S. (2005). "Strengthening in carbon nanotube/aluminium (CNT/Al) composites." *Scripta Materialia*, **53**, 1159-1163.
- Huang, C.S., Huang, B.R., Jang, Y.H., Tsai, M.S., and Yeh, C.Y. (2005). "Three-terminal CNTs gas sensor for N₂ detection." *Diamond & Related Materials*, **14**, 1872-1875.
- Jang, Y.-T., Moon, S.-H., Ahn, J.-H., Lee, Y.-H., and Ju, B.-K. (2004). "A simple approach in fabricating chemical sensor using laterally grown multi-walled carbon nanotubes." *Sensors and Actuators. B, Chemical*, **99**, 118-122.
- Korotcenkov, G. (2007). "Metal oxides for solid-state gas sensors: What determines our choice?" *Materials Science and Engineering: B*, **139**, 1-23.
- Kong, J., Franklin, N. R., Zhou, C., Chapline, M.G., Peng, S., Cho, K., and Dai, H. (2000). "Nanotube Molecular Wires as Chemical Sensors." *Science*, **287**, 622-625.
- Lee, W. and Park, S.-J. (2014). "Porous anodic aluminum oxide: anodization and templated synthesis of functional nanostructures." *American Chemical Society*, **114**, 7487-7556.
- Lin, H.-W., Chang, Y.-H., and Chen, C. (2012). "Facile Fabrication of TiO₂ Nanorod Arrays for Gas Sensing using Double-Layered Anodic Oxidation Method." *Journal of The Electrochemical Society*, **159**, K5-K9.
- Li, J., Lu, Y., Ye, Q., Cinke, M., Han, J., and Meyyappan, M. (2003). "Carbon Nanotube Sensors for Gas and Organic Vapor Detection." *Nano Letters*, **3**, 929-933.
- Liang, Y.X., Chen, Y.J., and Wang, T.H. (2004). "Low-resistance gas sensors fabricated from multiwalled carbon nanotubes coated with a thin tin oxide layer." *Applied Physics Letters*, **85**, 666-668.
- Modi, A., Koratkar, N., Lass, E., Wei, B., and Ajayan, P.M. (2003). "Miniaturized gas ionization sensors using carbon nanotubes." *Nature*, **424**, 171-174.
- Novoselov, K.S., Geim, A.K., Morozov, S.V., Jiang, D., Zhang, Y., Dubonos, S.V., Grigorieva, I.V., and Firsov, A.A. (2004). "Electric Field Effect in Atomically Thin Carbon Films." *Science*, **306**, 666-669.
- Ong, K.G., Zeng, K., and Grimes, C.A. (2002). "A wireless, passive carbon nanotube-based gas sensor." *IEEE Sensors Journal*, **2**, 82-88.
- Qi, P., Vermesh, O., Grecu, M., Javey, A., Wang, Q., Dai, H., Peng, S., and Cho, K.J. (2003). "Toward large arrays of multiplex functionalized carbon nanotube sensors for highly sensitive and selective molecular detection." *Nano Letters*, **3**, 347-351.
- Tang, H., Prasad, K., Sanjinés, R., and Lévy, F. (1995). "TiO₂ anatase thin films as gas sensors." *Sensors and Actuators. B, Chemical*, **26**, 71-75.
- Tomchenko, A.A., Harmer, G.P., Marquis, B.T., and Allen, J.W. (2003). "Semiconducting metal oxide sensor array for the selective detection of combustion gases." *Sensors and Actuators B: Chemical*, **93**, 126-134.
- Varghese, O.K., Kichambare, P.D., Gong, D., Ong, K.G., Dickey, E.C., and Grimes, C.A. (2001). "Gas sensing characteristics of multi-wall carbon nanotubes." *Sensors and Actuators. B, Chemical*, **81**, 32-41.
- Villalpando-Páez, F., Romero, A.H., Muñoz-Sandoval, E., Martínez, L.M., Terrones, H., and Terrones, M. (2004). "Fabrication of vapor and gas sensors using films of aligned CN_x nanotubes." *Chemical Physics Letters*, **386**, 137-143.
- Wagner, R.S. and Ellis, W.C. (1964). "Vapor-liquid-solid mechanism of single crystal growth." *Applied Physics Letters*, **4**, 89-90.
- Wong, Y.M., Kang, W.P., Davidson, J.L., Soh, A., and Wisitsora-at, K.L. (2003). "A novel microelectronic gas sensor utilizing carbon nanotubes for hydrogen gas detection." *Sensors and Actuators. B, Chemical*, **93**, 327-332.
- Xia, Y., Yang, P., Sun, Y., Wu, Y., Mayers, B., Gates, B., Yin, Y., Kim, F., and Yan, H. (2003). "One-dimensional nanostructures: synthesis, characterization, and applications." *Advanced Materials*, **15**, 353-389.
- Zhao, J., Buldum, A., Han, J., and Lu, J.P. (2002). "Gas molecule adsorption in carbon nanotubes and nanotube bundles." *Nanotechnology*, **13**, 195-200.